1 Fast, 3D isotropic imaging of whole mouse brain using multi-

2 angle-resolved subvoxel SPIM

3 Jun Nie[1+], Sa Liu[1+], Tingting Yu[2,3+], Yusha Li[2], Junyu Ping[1], Peng Wan[2], Fang Zhao[1],

4 Yujie Huang[4], Wei Mei[4], Shaoqun Zeng[2,3], Dan Zhu[2,3*] and Peng Fei[1,2*]

5 [1] School of Optical and Electronic Information, Huazhong University of Science and

6   Technology, Wuhan, 430074, China.

7 [2] Britton Chance Center for Biomedical Photonics, Wuhan National Laboratory for

8   Optoelectronics, Huazhong University of Science and Technology, Wuhan, 430074,

9   China.

10 [3] MoE Key Laboratory for Biomedical Photonics, Huazhong University of Science and

11   Technology, Wuhan, 430074, China

12 [4] Department of Anesthesiology, Tongji Hospital, Tongji Medical College, Huazhong

13   University of Science and Technology, Wuhan, 430030, China

14

15

16 Abstract

17 The recent integration of light-sheet microscopy and tissue-clearing has facilitated an

18 important alternative to conventional histological imaging approaches. However, the *in*

19 *toto* cellular mapping of neural circuits throughout an intact mouse brain remains highly

20 challenging, requiring complicated mechanical stitching, and suffering from

21 anisotropic resolution insufficient for high-quality reconstruction in three dimensions.

22 Here, we propose the use of a multi-angle-resolved subvoxel selective plane

23 illumination microscope (Mars-SPIM) to achieve high-throughput imaging of whole

24 mouse brain at isotropic cellular resolution. This light-sheet imaging technique can

25 computationally improve the spatial resolution over six times under a large field of view,

26 eliminating the use of slow tile stitching. Furthermore, it can recover complete

27 structural information of the sample from images subject to thick-tissue

28 scattering/attenuation. With Mars-SPIM, we can readily obtain a digital atlas of a

29 cleared whole mouse brain (~7 × 9.5 × 5 mm) with an isotropic resolution of ~2 μm (1

30 μm voxel) and a short acquisition time of 30 minutes. It provides an efficient way to

31 implement system-level cellular analysis, such as the mapping of different neuron

32 populations and tracing of long-distance neural projections over the entire brain. Mars-

33 SPIM is thus well suited for high-throughput cell-profiling phenotyping of the brain

34 and other mammalian organs.

35

36 **Introduction**

37 The comprehensive understanding of complex cellular connections in the whole

38 mammalian brain is one of the fundamental challenges in neuroscience. To unravel the

39 various neuronal profiles of different physiological functions in the whole brain, three-

40 dimensional (3-D) high-resolution imaging is required over a mesoscale sized volume[1,2].

41 However, creating such a large-scale brain dataset has posed a big challenge for current

42 3-D optical microscopy methods, all of which show relatively small optical

43 throughputs[3-5]. Furthermore, light scattering and attenuation are outstanding issues for

44 the turbid tissues that limit the extraction of signals from deep brain. To address these

45 issues, 3-D tile stitching combined with brain sectioning has been a popular strategy for

46 obtaining mammalian brain atlases, which can be a meaningful platform for mapping

47 neuronal populations, activities, or connections over the entire brain[6]. For example,

48   sequential two-photon (STP) microscopy can three-dimensionally image the brain at

49   subcellular high resolution[7-15], but at the cost of long acquisition times of up to several

50   days and a high-maintenance   system setup. The advent of light-sheet fluorescence

51   microscopy[16-22] (LSFM) in conjunction with tissue-clearing[23-28] eliminates the need for

52   complicated mechanical slicing of samples by instead applying nondestructive optical

53   sectioning. Although LSFM still needs repetitive image stitching to achieve high lateral

54   resolution over a large field of view (FOV), its use of wide-field detection results in

55   higher imaging speeds compared with the point-by-point scanning of epifluorescence

56   methods. A few well-known derivations of LSFM, for example, selective plane

57   illumination microscopy (SPIM), have recently been used for mouse brain imaging with

58   balanced speed and spatial resolution. However, the axial extent of the plane

59   illumination in SPIM has to be compromised to its lateral illumination FOV so that an

60   anisotropic axial resolution (typically of 5 to 20 μm, depending on the size of the mosaic

61   patch needing to be illuminated) can be yielded for whole-brain scale imaging[29,30]. As

62   a result, it is difficult to resolve fine neuronal structures and connections in three

63   dimensions, as can be achieved by conventional epifluorescence methods such as

64   micro-optical sectioning tomography[13,14] (MOST) and STP excitation microscopy[10-12].

65   Furthermore, even with the much larger imaging depth enabled by tissue clearing[30-33],

66   photon absorption and scattering still occur in the clarified tissues of whole mammalian

67   organs. These cause noticeable deterioration of signals from deep tissues. Recently,

68   multi-view fusion techniques[34-36], which have previously been used in the imaging of

69   small live embryos[37,38], have also been applied to excised mouse brains. These can

70   improve the relatively low axial resolution and suppress deep tissue scattering[39].

71   However, for the direct imaging of mesoscale intact organs, the lateral resolution of

72   SPIM systems, being 5 μm at its best, is insufficient to visualize single cells under a

73   large FOV of over 5 mm. In such circumstances, multi-view techniques cannot

74   overcome the lateral resolution limit determined by the detection optics. However, if

75   multi-view techniques were to be combined with repetitive image stitching, the

76   throughput advantage of LSFM would be significantly reduced, as well as the photon

77   utility.

78   Here, we present a whole-brain mapping pipeline, termed multi-angle-resolved

79   subvoxel SPIM (Mars-SPIM), which can image the whole mouse brain at an isotropic

80   voxel resolution of ~1 μm with a high throughput rate of half an hour per brain. This

81   imaging strategy combines our sub-voxel-resolving computation[40] with multi-view

82   Bayesian deconvolution[36,41] to achieve fast and accurate reconstruction of a whole brain

83   with isotropically improved resolution. Unlike conventional whole-brain imaging

84   methods that use stepwise z-scanning and 3-D tile stitching, Mars-SPIM directly

85   records low-resolution whole-brain images using a continuous non-axial scanning

86   method. This unique scanning mode provides a high acquisition rate, and meanwhile

87   encrypts sub-resolution shifts into raw images, which could be further processed by the

88   multi-view sub-voxel-resolving computation. Furthermore, this computation pipeline

89   is parallelized with multi-GPUs to achieve a high reconstruction throughput

90   (gigavoxels per minute) that matches the fast image acquisition. By reconstructing a

91   single-cell-resolution whole-brain atlas, we demonstrate successful brain-wide tracing

92   of single neural projections and the counting of different neuronal populations over the

93   entire brain. Mars-SPIM shows spatial-temporal performance superior to the other

94   available techniques for large-scale cell profiling, where sample size, spatial resolution,

95   and imaging throughput are all highly valued. It is therefore suitable for system-level

96   cellular analysis of brain or other whole organs.

97

98   **Results**

99   **Mars-SPIM setup and characterization**

100   We developed a Mars-SPIM system, with a low-profile setup with wide-FOV

101   illumination and detection sufficient to cover the entire mouse brain (see Methods and

102   Supplementary Figures 1 and 2). Under a certain view, the brain sample to be imaged

103   is continuously scanned across the laser-sheet along a non-axial direction. The camera

104   is synchronized to sequentially record a stack of plane images with a step-size

105   significantly smaller than the laser-sheet thickness. This non-axial scanning mode of

106   the Mars-SPIM encodes the low-resolution (LR) raw image stack with sub-voxel spatial

107   shifts, which are then used to reconstruct high-resolution (HR) images through the

108   application of an sub-voxel-resolving (SVR) algorithm (Supplementary Figure 3). The

109   sample is then rotated along the y-axis and non-axially imaged under multiple views

110   (Figure 1a). After the SVR computation has generated a series of HR images with

111   anisotropic volumes for all the views, a neuron-feature-based registration followed by

112   a multi-view Bayesian deconvolution (MVD) procedure is applied to accurately align

113   the multiple SVR volumes, compute their conditional probabilities, and finally produce

114   an output with recovered complete signals and isotropic super-resolution in three

115   dimensions. This SVR-MVD fused computation pipeline is further illustrated in Figure

116   1b and Supplementary Figure 3.

117   We used fluorescent microbeads with a diameter of ~500 nm as a point source to

118   characterize the Mars-SPIM system (Figure 1c and Supplementary Figure 4). For each

119   view, the microbeads were scanned by a ~12-μm thick (full width at half maximum

120   value; FWHM) laser-sheet with 280 nm step-size, and were detected by a 4×/0.16

121   objective. This non-axial scanning process (10 degrees to the x-z and y-z planes)

122   generated sub-resolution shifts of 48 and 272 nm in the lateral and axial directions

123   respectively. Thirty-four groups of LR image volumes representing the standard

124   resolution of the system optics (voxel size: $1.625 \times 1.625 \times 4.5$ μm) were extracted

125   from the raw image sequence to compute the HR images. The raw LR, single-view

126   SVR, conventional MVD, and SVR-MVD results are compared in Figure 1c. The line

127   intensity profiles of the resolved beads are plotted in Figure 1d and e, to indicate the

128   lateral and axial resolutions of these methods. The achievable lateral and axial FWHMs

129   of the SVR-MVD are improved from ~4.2 μm and 12 μm in the raw image to isotropic

130   values of ~1.4 μm, which are superior to both the single-view SVR (1.7 μm and 4.5 μm)

131   and conventional MVD (isotropic 3.4 μm).

132   We then demonstrated the imaging capability of the Mars-SPIM using clarified

133   brain tissue from a transgenic mouse (*thy1-GFP-M*). The brain sample was optically

134   sectioned by a 15-μm laser-sheet and imaged using a 4×/0.28 objective and a high-

135   speed camera (Hamamatsu Flash 4.0 v2) at a rate of 50 frames per second. The brain

136   sample was translated at a non-axial step-size of 280 nm (4 × 4 ×2 enhancement) and

137   rotated 45 degrees for each new view. Eight different view image stacks were rapidly

138   recorded in a total time of around 20 minutes. The raw image volume of each view was

139   acquired at the limited resolution of the system optics, and hence the densely-packed

140   neuronal fibers remained unresolvable (Figure 2a). The SVR procedure for each view

141   was then started with an initial guess, which was simply a ×4 interpolation of one of

142   the subdivided LR groups, and the process iteratively converged to the HR solution

143   (data not shown). Then, in the multi-view registration step, the neuronal cell bodies

144   were recognized as features to establish correspondences, instead of the beads. This

145   cell-based registration was verified to be as accurate as the bead-based one

146   (Supplementary Figures S5 and 6), while at the same time producing a cleaner

147   visualization (Supplementary Videos 1 and 2). Figure 2c shows the final Mars-SPIM

148   result with a reconstructed voxel size of 0.4 μm. This result is further compared with

149   conventional multiview SPIM (Mv-SPIM, Figure 2b), high magnification SPIM

150   (20×/0.45 with ~6.5-μm laser-sheet, Figure 2d) and confocal microscopy (10×/0.4,

151   Figure 2e). The linecuts through the transverse plane of the neuron dendrite (Figure 2a-

152   d) using each method reveal significantly improved resolution with the Mars-SPIM,

153   which surpasses both the 20×-SPIM result with anisotropic resolution in the

154   longitudinal direction, and the Mv-SPIM result with insufficient overall resolution

155   (Figure 2g). With the substantially enhanced isotropic resolution, two giant pyramidal

156   neurons could be finely segmented across a large volume (~400 gigavoxels for the

157   entire sample), as shown by the blue and red colors in Figure 2f and g. We note that

158 besides the increased space-bandwidth product (SBP; volume size divided by

159 resolution)[4,5], the Mars-SPIM also shows an improvement in the signal-to-noise ratio

160 (SNR), which can help to discern weak signals from the strong background signal of

161 thick tissue (Supplementary Figure 7). Furthermore, we tested different numbers of

162 views to verify that eight views formed a good balance between the data size/throughput

163 and performance (Supplementary Figure 8). Mars-SPIM can thus be considered as a

164 light-sheet microscope that is less vulnerable to spherical aberration and light scattering

165 in thick tissue, and combines a large FOV with high-resolution advantages that are

166 difficult to achieve with previous methods. From another perspective, the stitching-free

167 continuously-scanning mode exhibits a higher acquisition throughput than other

168 stitching-based methods, as well as lower photobleaching. In Figure 2h, we rate the

169 imaging performances of standard 4× SPIM, 20× SPIM, 10× confocal and our 4× Mars-

170 SPIM through comparisons of the system complexities, imaging speeds, photo-

171 bleaching rates, and spatial resolutions (also see Supplementary Figure 9 and

172 Supplementary Table 1). Compared with the confocal microscope (10×), the Mars-

173 SPIM gains advantages in imaging depth and axial resolution (Supplementary Figures

174 10 and 11). Besides the well-balanced volumetric resolution, the Mars-SPIM yields the

175 highest effective throughput at ~400 gigavoxels SBP in a 20-minute acquisition. Mars-

176 SPIM also eliminates the need for mechanical stitching, slicing, high-maintenance

177 optics, and precisely-modulated illumination, instead using a relatively simple light-

178 sheet setup and fast GPU-based computation to address the general challenge of high-

179 throughput high-resolution 3-D microscopy that was originally coupled to the physical

180   limitations of a system's optics. In the following whole-brain applications, this

181   underlying robustness allows the Mars-SPIM prototype to image the entire thick organ

182   with high spatial-temporal performance while maintaining a simple set-up.

183

184   **High-throughput, *in toto* imaging of whole mouse brain at high resolution**

185   An 8-week-old whole mouse brain (*Tg*: *thy1-GFP-M*) was optically cleared using the

186   a-uDISCO method[42], before being imaged by the Mars-SPIM. The brain shrank in size

187   from ~9.3 × 14 × 7.1 mm to ~7 × 9.5 × 5 mm after clearing (Figure 3a). Despite the use

188   of tissue clearing, light attenuation/scattering from deep tissue remained a big challenge

189   for the complete imaging of the whole brain (Supplementary Figure 13). However,

190   brain-wide biomedical applications such as cell population mapping and neuronal

191   projection tracing intrinsically need high spatial resolution across a large area, hence

192   highlighting the significance of the Mars-SPIM method. Experimentally, the whole

193   brain was imaged under a low-magnification setup of 25-μm light-sheet illumination

194   plus ×2.2 wide-field detection, and therefore only required to be stitched twice because

195   of the large FOV. The brain was then rotated for each view of the nonaxial scanning

196   (950 nm step-size, 5500 frames in 110 s), with a total of 16 views of raw stacks being

197   rapidly obtained in around half an hour. Using the above mentioned SVR-MVD

198   procedure, we successfully reconstructed the entire brain at an isotropic voxel size of

199   0.975 μm. Figure 3b shows a reconstructed volume rendering of the whole brain (400

200   gigavoxels, MIP mode). The horizontal planes (x-y) at different depths (Figure 3c-e)

201   and coronal planes (x-z) at different heights (Figure 3f-h) are extracted from the

202   reconstructed brain volume and compared with the conventional SPIM results. It is

203   obvious that the Mars-SPIM shows remarkable improvements in resolution, contrast,

204   and signal integrity. Vignettes of high-resolution Mars volumes of five selected areas

205   (Figure 4a), including the left and right cortex, hippocampus, thalamus and cerebellum,

206   are shown in Figure 4b-f respectively. The strong efficacy of the neural signal recovery,

207   as well as the resolution enhancement by Mars-SPIM, are further illustrated in

208   Supplementary Figure 13, in which a full coronal plane acquired by conventional SPIM

209   and experiencing strong scattering from both illumination (x) and emission (z) is

210   compared with the same plane acquired by Mars-SPIM. By quickly creating a cellular-

211   resolution brain atlas encompassing 400 gigavoxels across a large volume of over 300

212   mm^3 (post-computation time ~12 hours), the Mars-SPIM enables high-throughput

213   analysis of massive neurons at the whole brain level, which are otherwise spatially or

214   temporally more challenging using regular light sheet microscopes. (Figure 2h,

215   Supplementary Figure 14).

216

217   **Whole-brain visualization and segmentation**

218   Using the Mars-SPIM reconstruction of the whole brain (8-week-old mouse), we

219   explored the neuronal cyto-structures in various brain sub-regions, and precisely traced

220   the interregional long-distance projections of neurons which is crucial for

221   understanding the functionality of the brain (Figure 5, Supplementary Videos 3, 4 and

222   5). After the Mars-SPIM reconstruction of the whole brain, we used an adaptive

223   registration method[43-45] to three-dimensionally map the brain to the standard Allen

224   Brain Atlas (ABA). The brain was first re-oriented from horizontal view to coronal

225   view and automatically pre-aligned to the ABA using Elastix[43]. This pre-aligned brain

226   was then resized into LR and HR groups, as shown in Figure 5a step 2. Next, we finely

227   registered the LR group to the ABA, and obtained the transform correspondence (step

228   3), which was then applied to the HR group to obtain a registered and transformed HR

229   brain (step 4). This mapped brain atlas was finally visualized in Imaris to facilitate the

230   neuron analysis (Figure 5a).

231   With the creation of the atlas, the neurons localized to different encephalic regions

232   (such as cortex, hippocampus, cerebellum and midbrain) could be identified (Figure

233   5b), and *in toto* mapped out at a whole-brain scale (Figure 5c). Then, the neuron

234   population and the density in different encephalic regions were quantified by

235   calculating the volume of the regions and counting the identified cell bodies within

236   them (Figure 5d). The results show that among the 12 primary regions, the hippocampus

237   formation had the highest neuron density of 4600 cells/mm^3, which is consistent with

238   prior knowledge[46]. It should be noted that the current low-number counting results were

239   obtained using a *thy1-GFP-M* transgenic mouse, in which GFP signal is expressed by

240   less than 10% of all motor axons, retinal ganglion cells, lumbar dorsal root ganglions,

241   and cortex[47]. According to the registered HR images, we could trace the neuron

242   projections passing through different brain regions. The whole brain data were

243   volumetrically rendered with several sub-regions being segmented in different colors.

244   Figure 5e shows horizontal and coronal views of the volume renderings. The

245   trajectories of six long-distance (LD) projection neurons were successfully traced and

246 annotated in the digital whole-brain, revealing how they were broadcast across the

247 different regions of the brain (Figure 5f). Given the fact that this quantitative analysis

248 was implemented using a *thy1-GFP-M* mouse with a large number of neurons being

249 labeled, this procedure should be more efficient if the mouse brain were to be labelled

250 more specifically, such as with a virus tracer. Through the above mentioned

251 demonstration, we have shown the potential of our strategy for imaging-based

252 quantifications of the whole-brain, or other whole-organ-level analyses, which are

253 crucial for a variety of applications in histology, pathology, and neuroscience.

254

Discussion

256 Mars-SPIM can computationally surpass the resolution limit of a regular light-sheet

257 microscope and suppress the light scattering/attenuation that often exists in thick-tissue

258 imaging. Unlike mechanical slicing and tile stitching, which require complicated

259 operations, this strategy provides a simple and efficient way to achieve high-throughput

260 whole-brain mapping at a single-cell resolution. The use of simple optics in the Mars-

261 SPIM offers an ultra-large FOV of hundreds of mm^3, facilitating direct coverage of the

262 whole brain (or other whole organs). Its stitching-free continuous scanning mode

263 greatly reduces the acquisition time for such tissue volumes from several hours with

264 traditional methods to several minutes. Complementing the rapid data acquisition, a

265 highly GPU-parallelized SVR-MVD computation flow is followed to reconstruct the

266 super-resolved 3-D brain atlas at a high throughput time of a few hours. In our

267 demonstration, the quickly reconstructed digital mouse brain acquired by Mars-SPIM

268   presents an isotropic cellular resolution (~2 μm) with three- to ten-fold improvement in

269   resolution compared with conventional macro-view SPIM. It should also be noted that

270   this Mars-SPIM strategy can be applied to most existing light-sheet microscopes using

271   a simple retrofit, and can expand the optical throughput for fast, high-resolution

272   mapping of whole biological specimens without necessarily increasing the system

273   complexity. Thus, it can be characterized as a high-throughput 3-D imaging method

274   with a simple and cost-effective setup. Furthermore, the Mars-SPIM imaging in

275   conjunction with efficient brain registration can form a pipeline for creating an isotropic

276   whole-brain atlas, with which brain-wide quantitative analysis (e.g., neuron populations,

277   densities, and long-distance neuronal projections) could be easily implemented. In

278   combination with recent advances in specimen preparation techniques, such as

279   fluorescence-friendly tissue clearing, virus-based sparse labelling and transgenic

280   animal models, the Mars-SPIM could be more powerful in enabling various cellular

281   analyses of neural systems. Besides whole-brain mapping, we believe the Mars-SPIM

282   method could improve the efficiency of imaging other mammalian organs, such as lung,

283   kidney, and heart, and be of benefit for a wide variety of biomedical applications.

284   Furthermore, its ability to readily accomplish cellular imaging of mesoscale organisms

285   at hundreds of gigavoxel SBP renders Mars-SPIM a widely applicable tool for cellular

286   profiling, phenotyping, or sample screening assays in histology, pathology, and

287   developmental biology, in which both large-scale statistics and cellular details are often

288   desired for whole-tissue-level study.

289

Methods

Mars-SPIM imaging setup

A fiber-coupled DPSS laser (CNI laser, 488 nm, single-mode fiber) was used for excitation source. The laser was first collimated into a Gaussian beam with diameter ~3.3 mm (Thorlabs, F280FC-A). Then a sandwich structure containing a convex lens (f = 50 mm, Thorlabs, AC254-050-A) and two cylindrical lenses (f = 30 mm and 150 mm, Thorlabs, LJ1212L1, LJ1934L1) was designed to transform the round beam into an elliptical shape. The expansion ratio in short (x) and long (y) axis was ×0.6 and ×3, respectively, forming an elliptical beam with size of 10 by 2 mm (Supplementary Figure 2). A pair of adjustable mechanical slits (0-8 mm aperture, Thorlabs, VA100C/M) were placed orthogonally to further truncate the beam and thereby tune the height and thickness of the laser-sheet. The modulated elliptical beam was equally split into two parts via a 50/50 prism (Thorlabs, CCM1-BS014/M), to form two opposite beams, which will be further used to illuminate the sample from dual sides. A dual-side optical sectioning of the whole brain sample was finally formed by using two symmetric combination of cylindrical lens (Thorlabs, LJ1695RM) and illuminating objective (Olympus, 4×/0.10). The laser sheet had a widely tunable range from 5 to 50 μm in thickness and 0.5 to 10 mm in height.

Unlike regular detection setup applied in SPIM, we specially used a 4×/0.28 objective in conjunction with an ED Plan 1× tube lens to construct an infinity-corrected, wide-field, and large-aperture detection path (equivalent magnification ×2.2). Compared to the conventional infinity-corrected low-magnification detection, e.g, 2× Nikon

312   objective plus 200 mm focal length tube lens, this setup can collect much more

313   fluorescent signals under a large illumination range due to the larger aperture

314   (Supplementary Figure S9). A four-degree-of-freedom motorized stage (x, y, z

315   translation and rotation around the y-axis, Thorlabs and Phidgets Inc.) integrated with

316   a pair of customized tilting plates (10° inclined surface) was constructed for sample

317   mounting , rotating at multiple angle of views, and scanning across the laser sheet in an

318   off-detection-axis direction (Supplementary Figure S1). A digital camera (Hamamatsu

319   Orca Flash 4.0 v2 plus, or Andor Zyla 5.5) continuously records the images from the

320   consecutively illuminated planes at a high speed up to 50 full frames per second.

321

322   **Sample preparation**

323   Tissue clearing is an essential procedure before imaging. Here we used a-uDISCO

324   method to clear the brains of 8-weeks *thy1- GFP* mice (line M, Jackson Laboratory).

325   In the brain block experiment, to preserve the fluorescence and avoid photobleaching,

326   the cleared brain was embedded into a specific formulated resin[48], the refractive index

327   of which was equal to the index-matched immersion. For conducting bead-based

328   registration, fluorescent beads (Lumisphere, 1%w/v, 500 nm, SiO_2) were mixed around

329   the sample in the resin. 10 μl of bead stock solution was centrifuged at 1200 rpm for 3

330   minutes with the water-phase supernatant being removed and replaced with 20 μl

331   methanol.   Then the methanol-based bead solution was mixed into the resin to form

332   the bead-resin mixture, which was finally poured into a tube mold with the brain

333   specimen embedded. The tube containing beads, resin and sample was stored in a dark

334 place for 2-3 days till it was solidified for LSFM imaging. For the cell body-based

335 registration of brain block, the sample was directly embedded in the resin without the

336 procedure of mixing bead. For whole brain imaging, the brain was dissected with

337 keeping an ~5 mm long spinal cord (Figure 3a). After optical clearing, the sample could

338 be mounted to the stage via connecting the harden spinal cord with the beam shaft of

339 the rotating motor (Figure 3a).

340

341 **Multi-view imaging acquisition**

342 The brain samples were scanned under eight views. Each times of scanning was

343 executed along a non-axial direction with a step-size significantly smaller than the

344 thickness of light sheet. Under continuous scanning mode, this value was determined

345 by the scanning velocity and camera frame rate, varying from 0.3 μm (for brain block)

346 to 1 μm (for whole brain), depending on the optical configuration. The corresponding

347 acquisition time for total 8 views was around 20 and 30 minutes, respectively. The high

348 magnification SPIM images for comparison were obtained using 20× objective plus a

349 thinner light sheet of ~6.5 μm. Finally, hundreds of gigabyte raw images were

350 transferred to a high-capacity SSD RAID of the workstation via the camera link cable.

351

352 **SVR-MVD reconstruction**

353 SVR computation combined multi-view Bayesian deconvolution[41] was implemented to

354 achieve isotropic high-resolution reconstruction of whole mouse brain. Under each

355 view, a series of low-resolution image stacks were extracted from the oversampled raw

356   data[40]. All low-resolution stacks were correlated with each other in term of sub-voxel-

357   resolution displacements and spatially registered to a high-resolution image stack with

358   an oblique, sub-voxel shift. The multiple low-resolution images and an initial guess of

359   high-resolution image were input into a maximum-likelihood-estimation based

360   computation model to iteratively obtain a converged high-resolution image. This high-

361   resolution estimate was corrected into the final reconstruction by a voxel re-alignment,

362   which recovers the accurate shape of the sample. In practice, the SVR algorithm was

363   applied in parallel to quickly obtain resolution-enhanced results for all the views.

364   After SVR processing for each view, the resolution-enhanced results were regarded as

365   input for multi-view reconstruction in Fiji program. Similar with the bead-based

366   registration method[36], here the neuron cell bodies were recognized as fiducial makers

367   to establish the correspondences between each two views. Then all the SVR views

368   could be precisely registered using these correspondences. A multi-view Bayesian

369   deconvolution[36] was applied at the final step to rationally gather the information from

370   all the registered SVR views, and generate an output image with containing complete

371   sample information as well as enhanced isotropic resolution. An improved Richardson-

372   Lucy deconvolution was used to obtain the final deconvolved image with faster

373   convergence. Furthermore, this SVR-MVD computation procedure could be highly

374   parallelized with GPU-based acceleration. The whole processing time for an entire

375   brain atlas (400 gigavoxels) was ~12 hours on a workstation equipped with dual E5-

376   2630 CPU, quad Geforce 1080Ti GPU and 1T memory. This time consumption could

377   be further reduced with employing more powerful computation units.

378

Confocal microscope and UltraMicroscope imaging

380   The confocal images are taken by Olympus FV3000 under 10× objective, with a voxel

381   size of $0.8 \times 0.8 \times 2$ μm at 0.5 Hz (Supplementary figure 9, 10 and 11). The whole brain

382   images taken by commercial light-sheet microscope (UltraMicroscope, LaVision

383   BioTec) are acquired at 1.6× and 8× magnification, which take about 20 minutes and

384   450 minutes, respectively (Supplementary figure 14).

385

Software

387   The synchronization of scanning and acquisition was accomplished by LabVIEW

388   (National Instruments). The SVR processing was implemented by customized code and

389   computed with CUDA acceleration. The multi-view registration was processed in Fiji.

390   The planar x-z planes of PSFs were performed using ImageJ. The 3-D rendering of

391   PSFs were visualized by Amira (Visage Imaging). The visualizations of neuron imaging,

392   including planar projections, 3-D renderings, neuron tracing, were performed by Imaris

393   (Bitplane).

394

Acknowledgements

Author contributions

405   P.F. initiated the investigation, designed the project. J.N., S.L., Y.P., T.Y., and F.Z.

406   developed the programs, carried out the imaging experiments and implemented

407   quantifications. Y.L., W.M. and T.Y. prepared the samples and helped to analyze the

408   data. P.F., D.Z., and S.Z. contributed, refined the concept and wrote the paper.

409

Additional information

411   Correspondence and requests for materials should be addressed to feipeng@hust.edu.cn

412   (P.F.) or dawnzh@mail.hust.edu.cn (D.Z.).

413

Conflict of interest

415   The authors declare that they have no conflict of interest.

416

References

418   1   Miyamichi, K. *et al.* Cortical representations of olfactory input by trans-synaptic tracing. *Nature*
419   **472**, 191-196 (2011).
420   2   Lichtman, J. W. & Denk, W. The big and the small: challenges of imaging the brain's circuits.
421   *Science* **334**, 618-623 (2011).
422   3   Lohmann, A. W., Dorsch, R. G., Mendlovic, D., Ferreira, C. & Zalevsky, Z. Space–bandwidth
423   product of optical signals and systems. *JOSA A* **13**, 470-473 (1996).
424   4   Mendlovic, D. & Lohmann, A. W. Space–bandwidth product adaptation and its application to
425   superresolution: fundamentals. *JOSA A* **14**, 558-562 (1997).

426   5   Greenbaum, A. *et al.* Increased space-bandwidth product in pixel super-resolved lensfree on-
427   chip microscopy. *Scientific reports* **3**, 1717 (2013).

428   6   Mayerich, D., Abbott, L. & McCormick, B. Knife-edge scanning microscopy for imaging and
429   reconstruction of three-dimensional anatomical structures of the mouse brain. *Journal of*
430   *microscopy* **231**, 134-143 (2008).

431   7   Webb, R. H. Confocal optical microscopy. *Reports on Progress in Physics* **59**, 427 (1996).

432   8   Helmchen, F. & Denk, W. Deep tissue two-photon microscopy. *Nature methods* **2**, 932-940
433   (2005).

434   9   Svoboda, K. & Yasuda, R. Principles of two-photon excitation microscopy and its applications
435   to neuroscience. *Neuron* **50**, 823-839 (2006).

436   10   Nikolenko, V., Poskanzer, K. E. & Yuste, R. Two-photon photostimulation and imaging of
437   neural circuits. *Nature methods* **4**, 943-950 (2007).

438   11   Katona, G. *et al.* Fast two-photon in vivo imaging with three-dimensional random-access
439   scanning in large tissue volumes. *Nature methods* **9**, 201-208 (2012).

440   12   Economo, M. N. *et al.* A platform for brain-wide imaging and reconstruction of individual
441   neurons. *Elife* **5** (2016).

442   13   Gong, H. *et al.* Continuously tracing brain-wide long-distance axonal projections in mice at a
443   one-micron voxel resolution. *Neuroimage* **74**, 87-98 (2013).

444   14   Gong, H. *et al.* High-throughput dual-colour precision imaging for brain-wide connectome with
445   cytoarchitectonic landmarks at the cellular level. *Nature communications* **7** (2016).

446   15   Quan, T. *et al.* NeuroGPS-Tree: automatic reconstruction of large-scale neuronal populations
447   with dense neurites. *Nature methods* **13**, 51-54 (2016).

448   16   Huisken, J., Swoger, J., Del Bene, F., Wittbrodt, J. & Stelzer, E. H. Optical sectioning deep
449   inside live embryos by selective plane illumination microscopy. *Science* **305**, 1007-1009 (2004).

450   17   Keller, P. J., Schmidt, A. D., Wittbrodt, J. & Stelzer, E. H. Reconstruction of zebrafish early
451   embryonic development by scanned light sheet microscopy. *science* **322**, 1065-1069 (2008).

452   18   Planchon, T. A. *et al.* Rapid three-dimensional isotropic imaging of living cells using Bessel
453   beam plane illumination. *Nat Methods* **8**, 417-423 (2011).

454   19   Schmid, B. *et al.* High-speed panoramic light-sheet microscopy reveals global endodermal cell
455   dynamics. *Nature communications* **4**, 2207 (2013).

456   20   Keller, P. J., Ahrens, M. B. & Freeman, J. Light-sheet imaging for systems neuroscience. *nature*
457   *methods* **12**, 27-29 (2015).

458   21   Guan, Z. *et al.* Compact plane illumination plugin device to enable light sheet fluorescence
459   imaging of multi-cellular organisms on an inverted wide-field microscope. *Biomedical optics*
460   *express* **7**, 194-208 (2016).

461   22   Lee, J. *et al.* 4-Dimensional light-sheet microscopy to elucidate shear stress modulation of
462   cardiac trabeculation. *The Journal of clinical investigation* **126**, 1679 (2016).

463   23   Ertürk, A. *et al.* Three-dimensional imaging of solvent-cleared organs using 3DISCO. *Nature*
464   *protocols* **7**, 1983-1995 (2012).

465   24   Hama, H. *et al.* ScaleS: an optical clearing palette for biological imaging. *Nature neuroscience*
466   **18**, 1518-1529 (2015).

467   25   Tainaka, K. *et al.* Whole-body imaging with single-cell resolution by tissue decolorization. *Cell*
468   **159**, 911-924 (2014).

469   26   Zhu, D., Larin, K. V., Luo, Q. & Tuchin, V. V. Recent progress in tissue optical clearing. *Laser*

470   *& photonics reviews* **7**, 732-757 (2013).

471   27   Yu, T., Qi, Y., Gong, H., Luo, Q. & Zhu, D. Optical clearing for multiscale biological tissues.
472   *Journal of biophotonics* **11**, e201700187 (2018).

473   28   Qi, Y. *et al.* FDISCO: Advanced solvent-based clearing method for imaging whole organs.
474   *Science advances* **5**, eaau8355 (2019).

475   29   Dodt, H.-U. *et al.* Ultramicroscopy: three-dimensional visualization of neuronal networks in the
476   whole mouse brain. *Nature methods* **4**, 331 (2007).

477   30   Susaki, E. A. *et al.* Advanced CUBIC protocols for whole-brain and whole-body clearing and
478   imaging. *Nature protocols* **10**, 1709-1727 (2015).

479   31   Tomer, R., Ye, L., Hsueh, B. & Deisseroth, K. Advanced CLARITY for rapid and high-
480   resolution imaging of intact tissues. *Nature protocols* **9**, 1682-1697 (2014).

481   32   Pan, C. *et al.* Shrinkage-mediated imaging of entire organs and organisms using uDISCO.
482   *Nature Methods* (2016).

483   33   Cai, R. *et al.* Panoptic imaging of transparent mice reveals whole-body neuronal projections
484   and skull–meninges connections. Report No. 1546-1726, (Nature Publishing Group, 2018).

485   34   Swoger, J., Verveer, P., Greger, K., Huisken, J. & Stelzer, E. H. Multi-view image fusion
486   improves resolution in three-dimensional microscopy. *Optics express* **15**, 8029-8042 (2007).

487   35   Krzic, U., Gunther, S., Saunders, T. E., Streichan, S. J. & Hufnagel, L. Multiview light-sheet
488   microscope for rapid in toto imaging. *Nature methods* **9**, 730-733 (2012).

489   36   Preibisch, S., Saalfeld, S., Schindelin, J. & Tomancak, P. Software for bead-based registration
490   of selective plane illumination microscopy data. *Nature methods* **7**, 418-419 (2010).

491   37   Tomer, R., Khairy, K., Amat, F. & Keller, P. J. Quantitative high-speed imaging of entire
492   developing embryos with simultaneous multiview light-sheet microscopy. *Nature methods* **9**,
493   755-763 (2012).

494   38   Chhetri, R. K. *et al.* Whole-animal functional and developmental imaging with isotropic spatial
495   resolution. *Nat Methods* **12**, 1171-1178 (2015).

496   39   Liu, S. *et al.* Three-dimensional, isotropic imaging of mouse brain using multi-view
497   deconvolution light sheet microscopy. *Journal of Innovative Optical Health Sciences* **10**,
498   1743006 (2017).

499   40   Fei, P. *et al.* Subvoxel light-sheet microscopy for high-resolution high-throughput volumetric
500   imaging of large biomedical specimens. *Advanced Photonics* **1**, 016002 (2019).

501   41   Preibisch, S. *et al.* Efficient Bayesian-based multiview deconvolution. *nature methods* **11**, 645-
502   648 (2014).

503   42   Li, Y., Xu, J., Wan, P., Yu, T. & Zhu, D. Optimization of GFP fluorescence preservation by
504   modified uDISCO clearing protocol. *Frontiers in neuroanatomy* **12**, 67 (2018).

505   43   Klein, S., Staring, M., Murphy, K., Viergever, M. A. & Pluim, J. P. Elastix: a toolbox for
506   intensity-based medical image registration. *IEEE transactions on medical imaging* **29**, 196-205
507   (2010).

508   44   Renier, N. *et al.* Mapping of brain activity by automated volume analysis of immediate early
509   genes. *Cell* **165**, 1789-1802 (2016).

510   45   Yang, X. *et al.* High-throughput light sheet tomography platform for automated fast imaging of
511   whole mouse brain. *Journal of biophotonics* **11**, e201800047 (2018).

512   46   Murakami, T. C. *et al.* A three-dimensional single-cell-resolution whole-brain atlas using
513   CUBIC-X expansion microscopy and tissue clearing. *Nature neuroscience* **21**, 625 (2018).
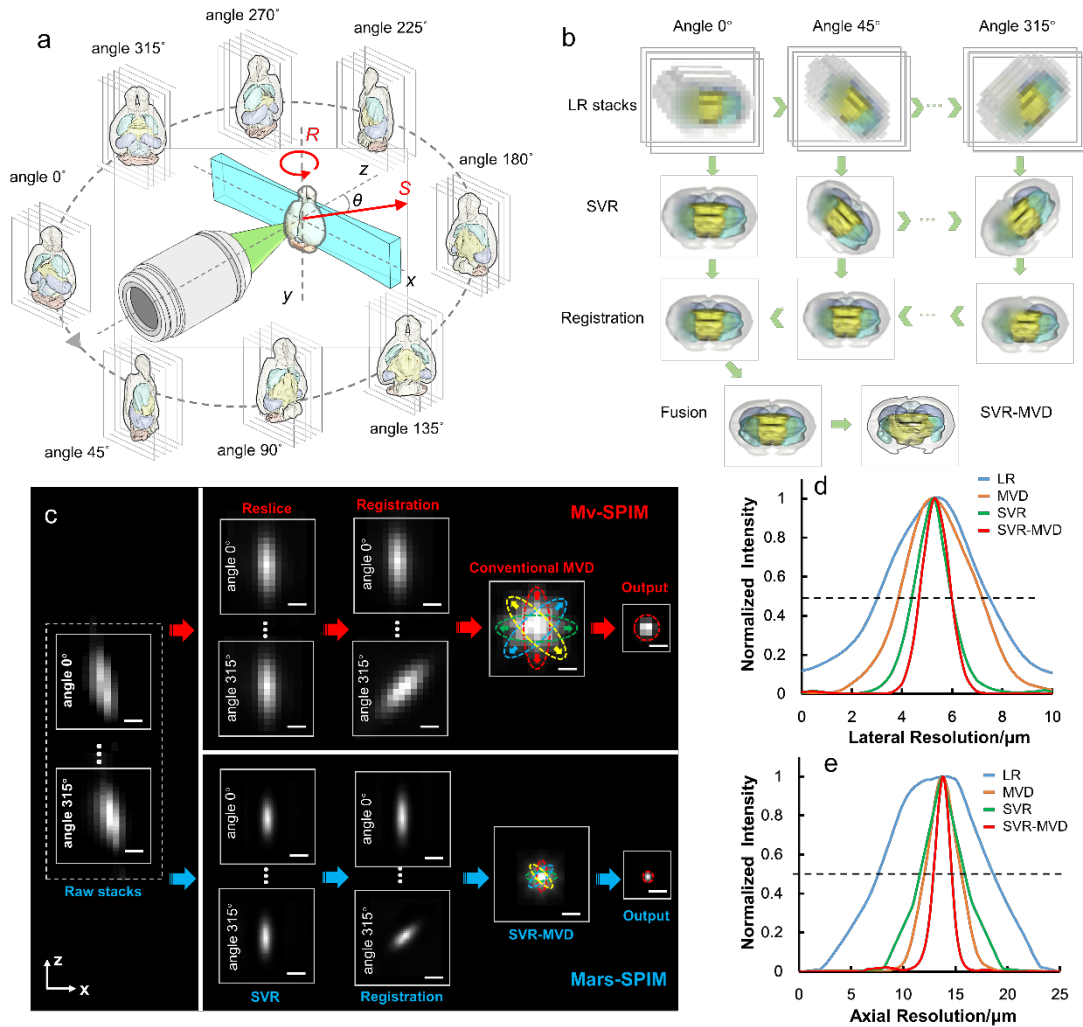
514   47   Feng, G. *et al.* Imaging neuronal subsets in transgenic mice expressing multiple spectral variants
515   of GFP. *Neuron* **28**, 41-51 (2000).
516   48   Becker, K. *et al.* Reduction of photo bleaching and long term archiving of chemically cleared
517   GFP-expressing mouse brains. *PloS one* **9**, e114149 (2014).

518

519

520 **Figures and Captions**

521

522 **Figure 1. Illustration and characterization of Mars-SPIM. (a)** The schematic of Mars-SPIM. A

523 low NA objective generates a relatively thick light-sheet and a low magnification objective collects

524 fluorescence with large FOV. The operation of the sample includes four degrees of freedom as: x

525 axis, y axis, non-axial direction s and rotation (along y axis). Unlike standard z-scan SPIM, here the

526 3-D scanning vector s (red) has a certain angle θ with respect to the x, y, z axes. This off-z-axis

527 scanning strategy in conjunction with a small step size encrypts the raw image stack with lateral and

528 axial sub-voxel-size shifts, which can be used to reconstruct a resolution-enhanced volumetric

529 image via SVR procedure. To suppress the light scattering from the deep tissues and achieve

530 isotropic 3-D resolution, the whole brain sample is rotated and imaged under eight views. **(b)** The

531   work flow of SVR-MVD procedure which can *in toto* reconstruct the whole brain at isotropically

532   enhanced resolution. It majorly includes: first, the SVR computation for multi-view, sub-voxel-

533   scanned raw images; second, feature-based registration of SVR-processed images; and third, a

534   Bayesian-based deconvolution that generates the final output based on multi-view SVR images. **(c)**

535   The resolution comparison between single-view raw image, SVR only, MVD only and SVR-MVD,

536   via resolving sub-resolution fluorescent beads (~500 nm diameter). x-z images show the lateral and

537   axial extents of the resolved beads (red circles). **(d)-(e)** The intensity plots of the linecuts through

538   the resolved beads along the lateral and axial directions, respectively. The SVR-MVD shows an

539   obviously highest isotropic resolution at ~1.4 μm, which is compared to ~4.2 (lateral) and 12 μm

540   (axial) in raw image. Scale bars: 5 μm in **(c)**.

541

542

543

544
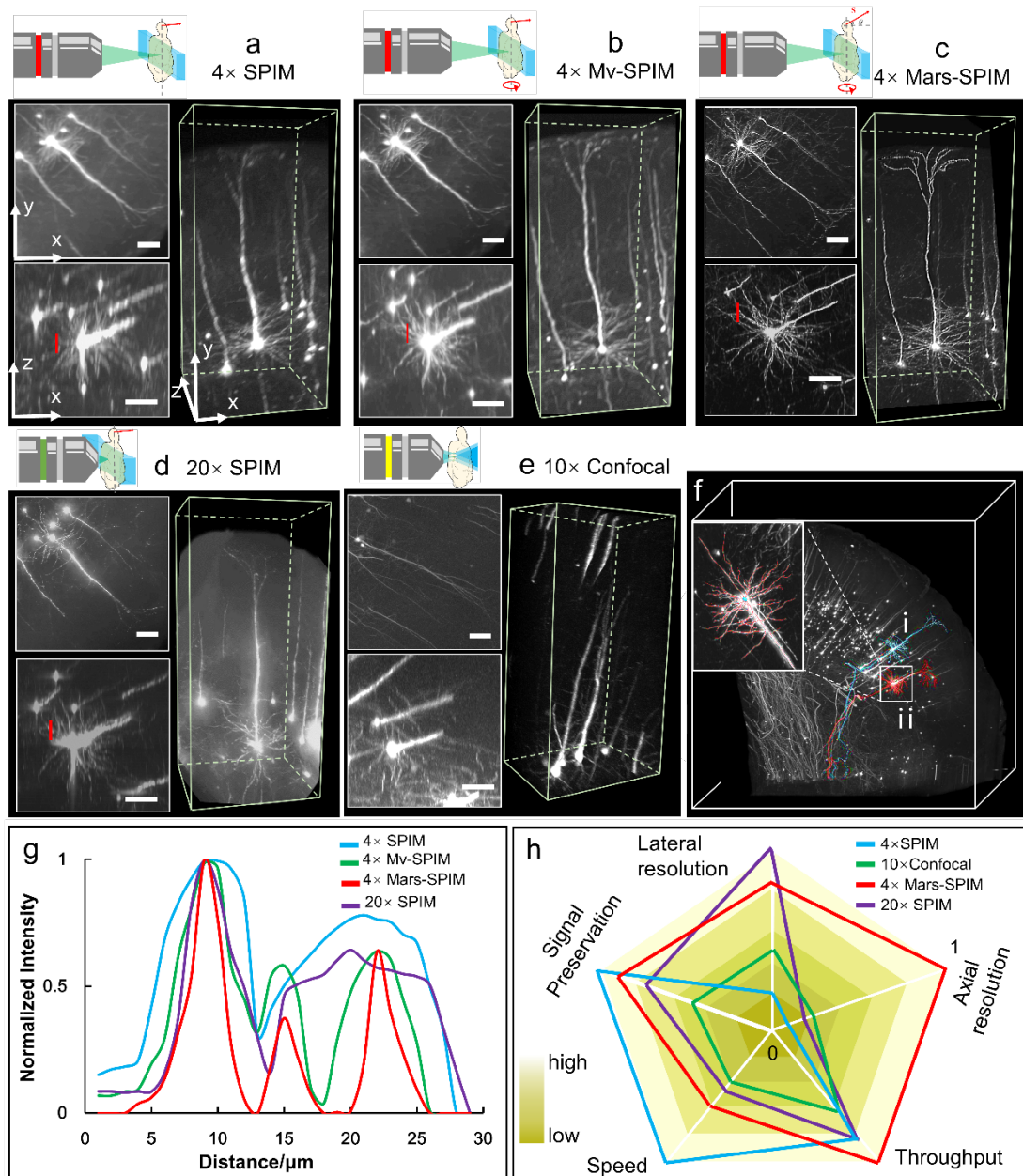
Figure 2. Mars-SPIM demonstration on *thy1-GFP-M* brain block. (**a**) Visualization of the neurons at cortex area by conventional SPIM using 4×/0.28 objective plus a 15 μm laser-sheet. The voxel size is 1.625 by 1.625 by 6 μm. (**b**) Conventional multiview SPIM (Mv-SPIM) results with an isotropic voxel size of 1.625*1.625*1.625 μm. (**c**) The Mars-SPIM results of the same neurons, with an isotropic reconstructed voxel size of 0.41*0.41*0.41 μm. (**d**) Comparison from high-resolution SPIM using 20×/0.45 air objective plus 6.5 μm light-sheet. Due to the increasing

551   spherical aberration under higher magnification, the SNR of the images is obviously decreased. **(e)**

552   The intensity plot of the dash lines transversely across a few neural fibers in **(a) - (d)**. It shows Mars-

553   SPIM has the narrowest peaks which indicate highest resolving power in practice. **(f)** The SVR-

554   MVD reconstruction of the entire brain block with size around 3 by 3 by 3 mm. As a result of finer

555   reconstruction, two pyramidal neurons with dendrites and axons are finely segmented, shown as **(i)**

556   and **(ii)**. **(g)** Vignette high-resolution view of the segmented neuron **(ii)** in **(f)**, showing the clearly

557   resolved fibers. **(h)** The radar map that compares the system simplicity, imaging throughput, photo-

558   bleaching, and spatial resolutions of four methods. The values are outputted by the logarithm and

559   normalized. Scale bars are 50 μm in **(a)-(e)**.

560
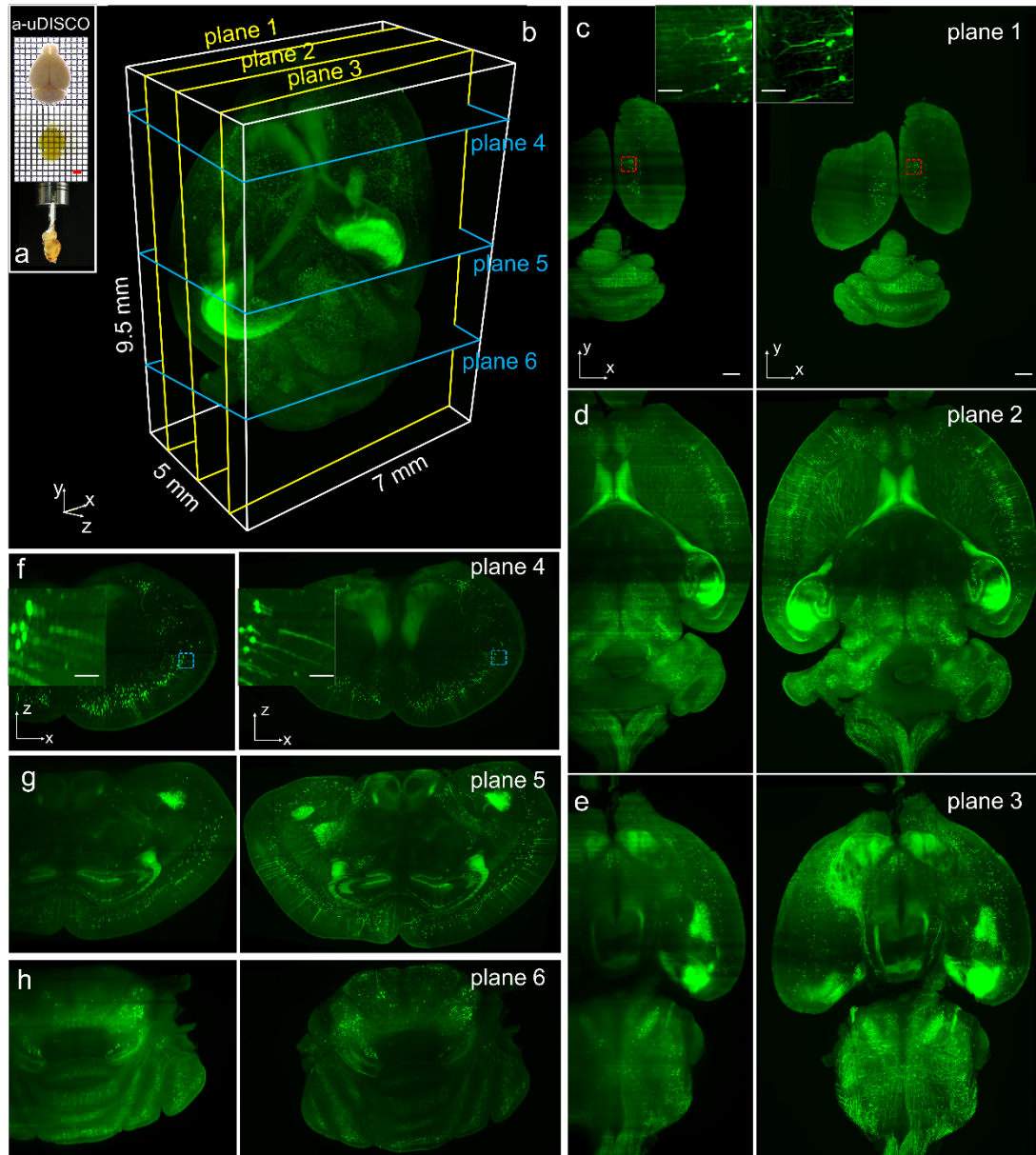
Figure 3. Comparison of whole mouse brain image by conventional SPIM and Mars-SPIM.

(a) The photographs of an adult mouse brain (8 weeks) before and after a-uDISCO clearing. **(b)** The 3D reconstruction of cleared whole mouse brain. With obtaining optically cleared brain for light-sheet imaging, our Mars-SPIM system rapidly provides 3D visualization of entire brain via SVR-MVD reconstruction (400 gigavoxels). Under each view, the sample is imaged using 2.2× magnification plus ~25 μm laser-sheet. The sub-voxel scanning step size is ~1 μm. The final result is recovered from raw images of eight views, with reconstructed isotropic voxel size of 1 by 1 by 1

569   μm. The imaging throughput here is ~30 minutes per whole brain, and the post-processing time is

570   ~12 hours with employing quad NVIDIA graphical cards. **(c)-(e)** compare the transverse (xy) planes

571   at 500, 2500 and 4000 μm z-depth, by conventional SPIM and Mars-SPIM. Mar-SPIM shows more

572   uniform image quality at the deep of tissue. **(f)-(h)** correspondingly compare the reconstructed

573   coronal (xz) planes at the height of 1500, 4000 and 8000 μm. The completely blurred parts by tissue

574   scattering/attenuation are discarded in conventional SPIM images. Besides the reconstruction

575   integrity of whole brain, the insets in **(c)-(e)** and **(f)-(g)** further compares the achieved lateral and

576   axial resolutions of regular SPIM images and Mars-SPIM images with using the same optics. Scale

577   bars: 500 μm in **(b)-(g)** and 100 μm in insets.

578

579

580
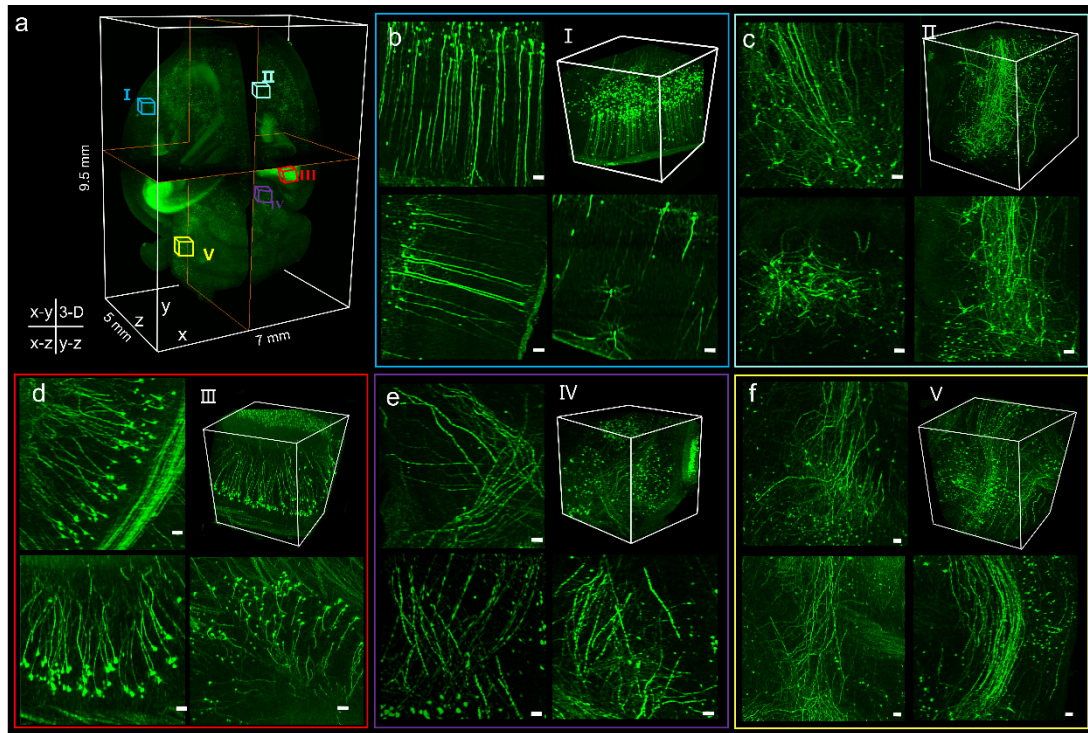
Figure 4. High-throughput, whole-brain imaging at isotropic cellular resolution using Mars-SPIM. (a) The reconstructed whole mouse brain by Mars-SPIM. Five selected volumes **(I-V)** at left cortex (blue), right cortex (cyan), hippocampus (red), thalamus (purple) and cerebellum (yellow) are shown in **(b)-(f)**, respectively, with each one containing the transverse (x-y), sagittal (y-z), coronal (x-z) planes and 3-D rendering of the selected volume. The neuronal cell bodies together with the projecting fibers can be identified as a result of significantly enhanced resolutions by Mars-SPIM. Scale bars: 20 μm in **(b)-(f)**.

588

589

590

591
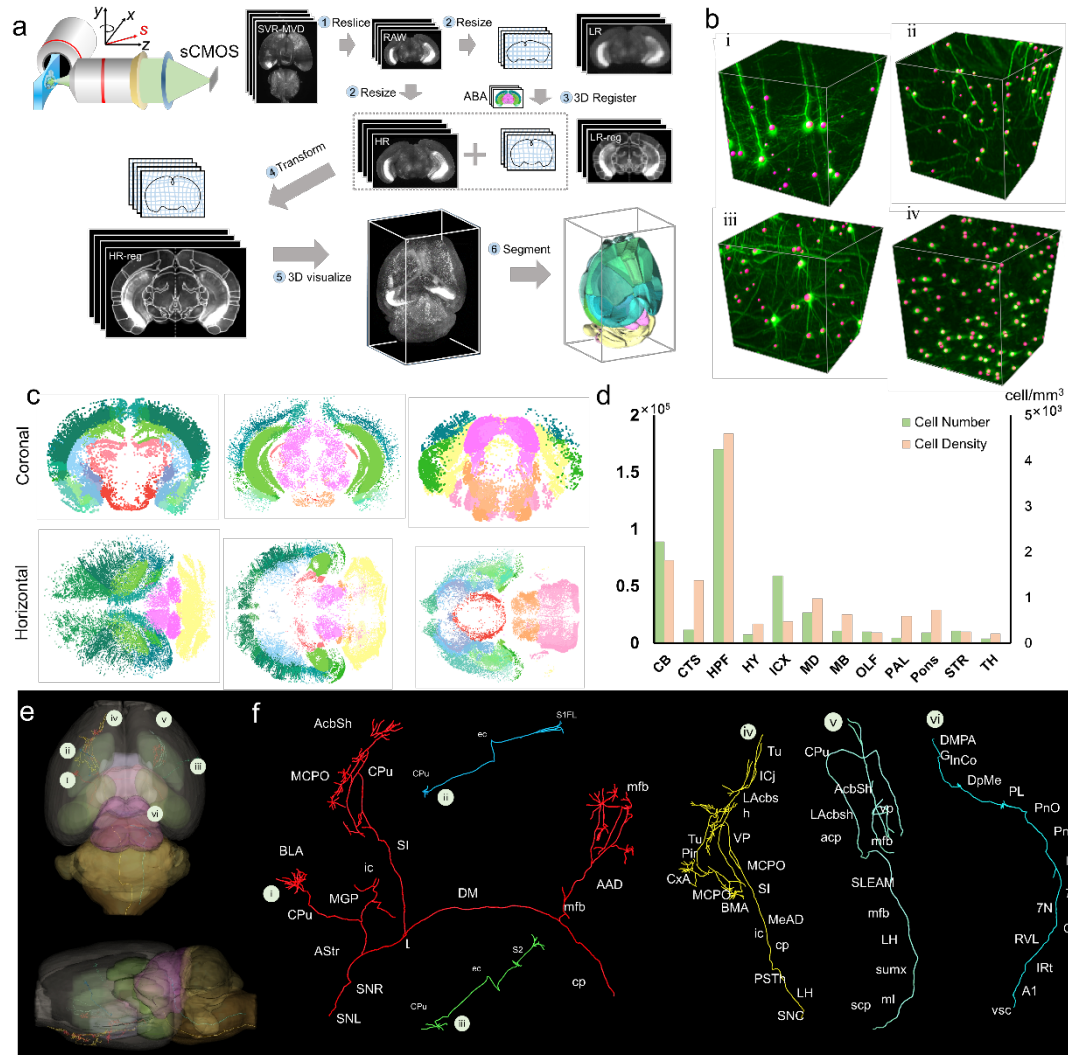
Figure 5. Quantifications of a *thy1-GFP-M* mouse brain based on Mars-SPIM image. (a) The

quick creation of whole brain atlas. Step 1: re-orientation of the Mars-SPIM image from horizontal

to coronal view and pre-alignment to standard Allen brain atlas (ABA) using Elastix. Step 2: resizing

the pre-aligned coronal images into low-resolution (LR) and high-resolution (HR) groups. Step 3:

registration of LR group to ABA to obtain the transformation matrix. Step 4: Application of the

transformation matrix to HR group to obtain the registered HR images. Step 5: 3D visualization of

the ABA-registered brain. Step 6: Segmentation of the brain regions in Amira. **(b)** With isotropic

single-cell resolution at whole-brain scale, 3D detection of single neurons can be readily achieved

at various brain regions. As a result, the neuron distribution at different regions of the whole brain

601   can be mapped out, as shown in the coronal and transverse views in (c). Each color represents a

602   brain region. **(d)** The neuron population and density calculated at 12 primary brain regions. CB,

603   cerebellum; CTS, cortical subplate; HPF, hippocampal formation; HY, hypothalamus; ICX,

604   isocortex; MD, medulla; MB, midbrain; OFL, Olfactory areas; PAL, pallidum; Pons, pons; STR,

605   striatum; TH, thalamus. **(e)** Horizontal and coronal views of the traced neuron long-distance

606   projections shown in volumetric rendering. **(f)** The pathway annotations of 6 long-distance

607   projection neurons. Abbreviations: AAD, anterior amygdaloid area, dorsal part; Acbsh, accumbens

608   nucleus, shell; Astr, amygdalostriatal transition area; BLA, basolateral amygdaloid nucleus, anterior

609   part; cp, CPu, caudate putamen (striatum); DM, ic, LH, lateral hypothalamic area; MCPO,

610   magnocellular preoptic nucleus; mfb, medial forebrain bundle; MGP, medial globus pallidus

611   (entopeduncular nucleus); SI SNL, substantia nigra, lateral part; SNR, substantia nigra, reticular

612   part; Tu, olfactory tubercle; ICj, islands of Calleja; LAcbsh, lateral amygdaloid nucleus; VP, ventral

613   pallidum; Pir, piriform cortex; CxA, cortex-amygdala transition zone; MCPO, magnocellular

614   preoptic nucleus; SI, substantia innominate; BMA, basomedial amygdaloid nucleus, anterior part;

615   MeAD, medial amygdaloid nucleus, anterior dorsal; ic, internal capsule; cp, cerebral peduncle, basal

616   part; PSTh, parasubthalamic nucleus; LH, lateral hypothalamic area; SNC, substantia nigra,

617   compact part; vsc, ventral spinocerebellar tract; A1, A1 noradrenaline cells; IRt, intermediate

618   reticular nucleus; RVL, rostroventrolateral reticular nucleus; C1, C1 adrenaline cells; 7N, facial

619   nucleus; 7DI, facial nucleus, dorsal intermediate subnucleus; PnC, pontine reticular nucleus, caudal

620   part; PnO, pontine reticular nucleus, oral part; PL, paralemniscal nucleus; DpMe, deep

621   mesencephalic nucleus; InCo, intercollicular nucleus; DMPAG, dorsomedial periaqueductal gray;

622   S1FL, primary somatosensory cortex, forelimb region; CPu, caudate putamen; ec, external capsule;

623   S2, secondary somatosensory cortex; scp, superior cerebellar peduncle; ml, medial lemniscus; sumx,

624   supramammillary decussation; LH, lateral hypothalamic area; mfb, medial forebrain bundle;

625   SLEAM, sublenticular extended amygdala, medial part; acp, anterior commissure, posterior; AcbSh,

626   accumbens nucleus, shell; vp, ventral pallidum;

627

628

629